Journal of Materials Chemistry A

COMMUNICATION

View Article Online
View Journal | View Issue

Cite this: J. Mater. Chem. A, 2025, 13, 6342

Received 4th December 2024
Accepted 6th February 2025

DOI: 10.1039/d4ta08604j

rsc.li/materials-a

Characterization of densification behavior and mechanical properties of solid electrolyte powders for all solid-state batteries†

Seung-Yong Lee, ‡[a] Ji-Hoon Han, ‡[bc] Hyun-Woo Gong,[d] Jae-pyoung Ahn,[d] Kyung-Woo Yi[b] and Young Whan Cho *[c]

A simple powder compression method was used to compare the mechanical properties of various argyrodite-type solid electrolytes. The Heckel plot's K values revealed differences in plastic deformation behavior, aligning qualitatively with nano-indentation test results.

All solid-state lithium batteries (ASSBs) have received great attention as next-generation batteries due to higher energy density and safety, in comparison with commercial lithium-ion batteries (LIBs).[1,2] Unlike LIBs consisting of liquid-electrolytes, ASSBs use solid-electrolytes (SEs), which play the role of separators together with the intermediate medium for ion-transport between the anode and cathode. Generally, four types of SEs have been reported such as sulfides, oxides, halides, and polymers. Each has its own advantages and disadvantages.[3]

Among these, sulfide-based solid electrolytes have garnered the most attention due to their ease of formability and high ionic conductivity, making them close to commercialization. Various sulfide solid electrolytes, such as lithium argyrodite, have been studied so far; however, most of the research studies have focused on the energy performance aspect, such as ionic conductivity and electrochemical stability, with less attention to their mechanical properties related to physical compatibility with electrodes.[4,5] Given that sulfide-based SEs can function both as a separator and an ion transport medium simply through the application of pressure at room temperature, the mechanical properties of the powder hold significant importance.[6,7] SEs should comply with the applied force, especially compressive stress, during the manufacturing process, in which ASSB cells are manufactured with sufficient pressure to minimize residual voids and to maximize the solid–solid contact interface between the SE and the anode/cathode materials for lithium-ion transportation.[8–10] The stress compliance of SEs is also significant under in-service conditions; the lattice contraction and expansion of electrode materials due to lithium-ion transportation during charge/discharge cycles can induce residual stress/strain on the solid–solid interfaces.[11–15] Given that SEs have less ability for stress compensation, the residual stress/strain could result in microvoid/crack formation at the interfaces, leading to the degradation of ASSB performance.[16–18] Recent research has reported that good stiffness of SEs enables compensation for the volume contraction/expansion of electrode materials effectively, minimizing internal charge transfer resistance induced by cracks and voids.[1,5,8,11–15,19–23] These findings emphasize that the microstructure and mechanical properties of solid electrolytes are critical to achieving higher stability and performance in ASSLMBs by mitigating dendrite-induced short-circuit failures.

Accordingly, mechanical properties of SEs must be considered for the development and application of ASSBs. In previous studies,[24–26] lattice elastic coefficients of SEs at the atomic-scale have been calculated through atomistic simulations. In actual manufacturing and in-service processes, however, macroscopic compressibility of SEs due to particle–particle and particle–void interactions will be more critical. In this study, comparative research was conducted on various sulfide SEs to evaluate stress compatibility by means of compression testing as well as by nano-indentation.

To understand the fundamentals of compression behavior of SE powders, the results of the representative commercial SE powder, Li_6PS_5Cl, are presented in Fig. 1. Fig. 1a indicates the total displacement (Δd) curve corresponding to the compressive stress (σ) and the inset shows the mold compression system with digital image correlation (DIC) analysis where the upper and lower plungers are speckle-patterned with SiO_2 particles on

[a]Materials Characterization Center, Korea Institute of Materials Science (KIMS), Changwon 51508, Republic of Korea
[b]Department of Materials Science and Engineering, Seoul National University, Seoul 08826, Republic of Korea
[c]Center for Hydrogen Energy Materials, Korea Institute of Science and Technology (KIST), Seoul 02792, Republic of Korea. E-mail: oze@kist.re.kr
[d]Advanced Analysis Center, Korea Institute of Science and Technology (KIST), Seoul 02792, Republic of Korea

† Electronic supplementary information (ESI) available. See DOI: https://doi.org/10.1039/d4ta08604j

‡ These authors contributed equally to the preparation of this manuscript.

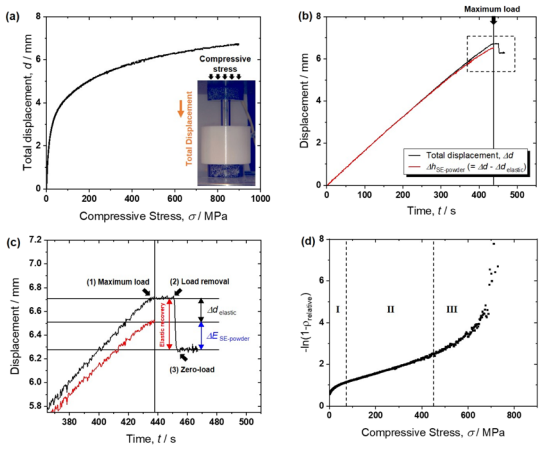

Fig. 1 (a) The total displacement (Δd) curve corresponding to the compressive stress (σ). (b) Δd and $\Delta h_{\text{SE-powder}}$ with time for commercial Li_6PS_5Cl powder. (c) The magnified image of the dotted line square segment in (b). (d) The negative natural logarithmic $(1 - \rho_{\text{relative}})$ *vs.* the compressive stress curve of the commercial Li_6PS_5Cl powder.

carbon tape (see the ESI† section for further details regarding DIC). Compressive force is applied on the upper plunger, which moves down toward a zirconia mold, and then the displacement is quantitatively measured in real-time by tracking the distance variation between the upper and lower plungers by DIC analysis. The total displacement rapidly increases and then appears saturated with increasing compressive stress. Variation of the displacement is closely related to the reduction of the mold space volume filled with SE powders and voids. However, one should be cautious that the displacement is also affected by the elastic contribution of the plunger rod.

The total displacement, Δd, under compressive load can be expressed as eqn (1);

$$\Delta d = \Delta d_{\text{elastic}} + \Delta h_{\text{SE-powder}} = \sigma L/E + \Delta h_{\text{SE-powder}} \quad (1)$$

where $\Delta d_{\text{elastic}}$ and $\Delta h_{\text{SE-powder}}$ are the elastic contribution of the plunger rod and the displacement of the height of the SE pellet, respectively. $\Delta d_{\text{elastic}}$ corresponds to $\sigma L/E$ where L is the length of the plunger rod (=40 mm) and E is the elastic modulus of the plunger material that was measured to be about 180 GPa by means of DIC analysis, which is comparable with the references.[27–30] Δd and $\Delta h_{\text{SE-powder}}$ with time for a commercial Li_6PS_5Cl sample are presented in Fig. 1b. It clearly shows that $\Delta d_{\text{elastic}}$, corresponding to the gap between two curves, gradually increases with time (load). This means that $\Delta d_{\text{elastic}}$ must be considered to measure the pellet height precisely, and DIC analysis is very effective in the case of in-die powder compression testing. Fig. 1c indicates the magnified image of the dotted line square segment in Fig. 1b. After reaching the maximum load (1), the applied load is removed at the point (2) and then the total displacement abruptly drops to the point (3). It can be regarded that the difference between (2) and (3) is the elastic recovery because there is no appearance of irreversible deformation such as cracks on the surface of the pellet. The elastic recovery is separated into two components; one is the elastic contribution of the plunger rod corresponding to the gap between both black and red curves (black double headed arrow) and the other is the elastic contribution of the pelletized SE powder sample, $\Delta E_{\text{SE-powder}}$ (blue double headed arrow).

SE powder undergoes various stages during powder-to-pellet formation under compression, such as powder rearrangement and plastic and/or elastic deformation.[31] To understand the compaction behavior of powders, the Heckel equation is widely used in various fields, especially in pharmaceutical powder compaction processes.[32–37] Assuming that the particle-to-pellet formation under compression is derived from a first-order chemical reaction, where the voids are the reactants and the densification of the solid is the product, the Heckel equation is expressed as eqn (2);

$$\ln\left\{\frac{1}{(1-\rho_{\text{relative}})}\right\} = K\sigma + A \quad (2)$$

where ρ_{relative} is the relative density of the pellet, K is the slope in the linear section of the stage II, and A is the intercept, respectively. Fig. 1d shows the negative natural logarithmic $(1 - \rho_{\text{relative}})$ *vs.* the compressive stress curve of the commercial Li_6PS_5Cl powder. Three different stages appear with increasing compressive stress. It is reported[35] that each stage is associated with the behavior of particles; stage I represents the initial curved region at lower pressure and it is related to particle rearrangement and/or fragmentation. Stage II represents the linear region at medium pressure where particles undergo mainly plastic deformation, and finally stage III shows the terminal curved region at higher pressure where elastic deformation of the dense compact mainly occurs.[32–34]

Fig. 2 shows the negative logarithmic $(1 - \rho_{\text{relative}})$ *vs.* compressive stress curves of various SE powders. The Heckel plots of as-received commercial Li_6PS_5Cl together with that of the same powder after ball-milling are shown in Fig. 2a. The value of K in stage II of as-received commercial Li_6PS_5Cl powder is 32.3 ($\times 10^{-4}$) and after ball milling, it slightly increases to 34.0 ($\pm$0.15). It is, however, noted that the ball-milled powder densifies relatively easily compared with the as-received powder. When compared to as-received commercial Li_6PS_5Cl powder (brown squares), the transition from stage II to III occurs at lower stress with the ball-milled commercial powder (purple circles). The compressive stress at 97% theoretical density of ball milled powder is 570 MPa while that of as-received powder is 650 MPa. It seems that as the particle size decreases, the voids are quickly filled with particles even under

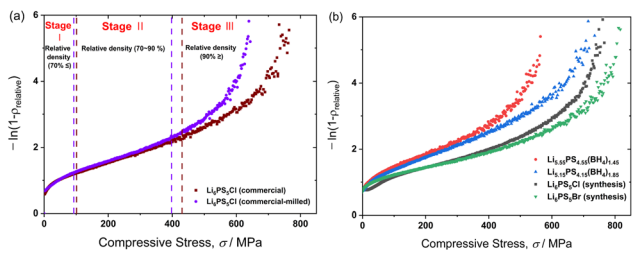

Fig. 2 (a) The Heckel plots of commercial Li_6PS_5Cl with that of the same powder after ball-milling (vibrating mill). The pressure required to reach each stage is different for each electrolyte. (b) The Heckel plots of various argyrodite solid electrolyte powders.

lower stress and thus densification of the pellet is accelerated, resulting in a reduced plastic deformation region (stage II) and an earlier transition to stage III. The milled powder approaches the theoretical density at significantly lower stress relative to as-received commercial powder while the K is approximately the same between these two powders. Given that the K is predominantly governed by intrinsic mechanical properties, such as the elastic modulus and/or plasticity, it is not uncommon to observe a comparable slope in SE powders with identical chemical compositions and crystal structures. When there is a significant difference in the morphology and/or size of the SE powders, however, it is natural to have different compacting behavior even if they have the same chemical composition and crystal structure.

When Cl^- in Li_6PS_5Cl is replaced with Br^-, the transition from stage II to III is delayed as shown in Fig. 2b. It is believed that the difference in the Heckel plot between Li_6PS_5Cl and Li_6PS_5Br is mainly derived from the change in the intrinsic mechanical properties of electrolyte itself, such as the elastic modulus and/or plasticity.[32,33,36,37] As shown in Table 1, the compressive stress at 97% of the theoretical density of the Li_6PS_5Cl compact is lower than that of Li_6PS_5Br, which agrees well with the above result that the transition between stage II and III appears at relatively lower stress with Li_6PS_5Cl compared to Li_6PS_5Br.

The Heckel plots of BH_4^- substituted SE powders are also presented in Fig. 2b. Compared to Li_6PS_5Cl powder, the transition from stage II to III of these SE powders tends to accelerate. In the initial densification stage, the voids are large enough for the particles to simply rearrange and gradually fill them up. As the voids become smaller than the average particle size, however, particles have to change their shape or even break into smaller ones through plastic deformation or fragmentation to fill up the remaining empty spaces. The plastic deformation behavior is controlled by the yield strength and elastic modulus. In eqn (1) representing the Heckel plot, the K value represents the linear section in stage II and indicates the stress compatibility of the powders. The reciprocal of the K value physically represents a quantity proportional to the yield strength of the powder.[32,33] K values derived from the Heckel plot in Fig. 2b are presented in Table 1. Li_6PS_5Br has a lower K value compared to Li_6PS_5Cl. K values of BH_4^- substituted powders are much higher than those of Li_6PS_5Cl and Li_6PS_5Br. In addition, the compressive stresses at 97% theoretical density are much lower than those of Li_6PS_5Cl and Li_6PS_5Br. The K value will mainly depend on the chemical composition, which is closely related to the change in the yield strength. This indicates that it is much easier for BH_4^- substituted SE powders to plastically deform to produce a compact of near theoretical density at room temperature compared with common halide substituted argyrodites such as Li_6PS_5Cl and Li_6PS_5Br.

The elastic modulus (E) and hardness (H) are critical mechanical properties that govern the deformation behavior of materials. The elastic modulus reflects the stiffness of a material and its ability to resist elastic deformation under stress, while hardness indicates resistance to localized plastic deformation.[38–41]

To further characterize the mechanical properties of SE powders, the indentation hardness and elastic modulus of the pellets were measured using nano-indentation, and the results are shown in Table 2. For the measurements, the pellets were compressed close to the theoretical density, as determined from the Heckel plots. The surface morphology of the ion milled SE powder compacts for the nano-indentation test is shown in Fig. 3. There are some pores but the porosity measured by an image analysis method is not higher than 7%. The nano-indentation curves of Li_6PS_5Br are also given in Fig. 3e and f. While the elastic modulus of Li_6PS_5Cl is slightly higher than that of Li_6PS_5Br, the hardness of Li_6PS_5Br is higher than that of Li_6PS_5Cl. This suggests that the yield stress of Li_6PS_5Cl is lower than that of Li_6PS_5Br. This result agrees with those from the Heckel plot as the K of Li_6PS_5Cl is higher than that of Li_6PS_5Br. Both the elastic modulus and indentation hardness of the BH_4^- substituted SE powders are much lower compared to those of Li_6PS_5Cl and Li_6PS_5Br.

The lower elastic modulus and hardness of BH_4^--substituted SEs result in earlier onset of plastic deformation under lower applied stress. This behavior facilitates efficient densification of the material by allowing voids to be filled with less energy, as shown in the Heckel plots and nano-indentation tests. This

Table 1 Slope K of the Heckel plot in stage II and compressive stress at 97% TD of SE powders. Because the y-axis of the Heckel plot uses the natural logarithm, the variation in compressive strength increases significantly as the density approaches 100% TD. Therefore, 97% was arbitrarily selected, as this density is close enough to TD, while the error range due to data fluctuations remains within an acceptable value

	Li_6PS_5Br	Li_6PS_5Cl	$Li_{5.15}PS_{4.15}(BH_4)_{1.85}$	$Li_{5.55}PS_{4.55}(BH_4)_{1.45}$
Slope, K ($\times 10^{-4}$ MPa^{-1})	25.0 ($\pm$0.16)	29.1 ($\pm$0.14)	37.0 ($\pm$0.11)	41.3 ($\pm$0.11)
Compressive stress @ 97% theoretical density (MPa)	725	675	570	510

Table 2 Nano-indentation results of various SE powders

	Li_6PS_5Br	Li_6PS_5Cl	$Li_{5.15}PS_{4.15}(BH_4)_{1.85}$	$Li_{5.55}PS_{4.55}(BH_4)_{1.45}$
Hardness (GPa)	1.68 ($\pm$0.11)	1.41 ($\pm$0.24)	0.69 ($\pm$0.07)	0.66 ($\pm$0.05)
Elastic modulus (GPa)	30.5	27.6	15.6	19.1
Porosity (%)	2.5	2.5	7.3	4.7
H/E (plasticity index) $\times 10^{-2}$	5.5	5.1	4.4	3.5

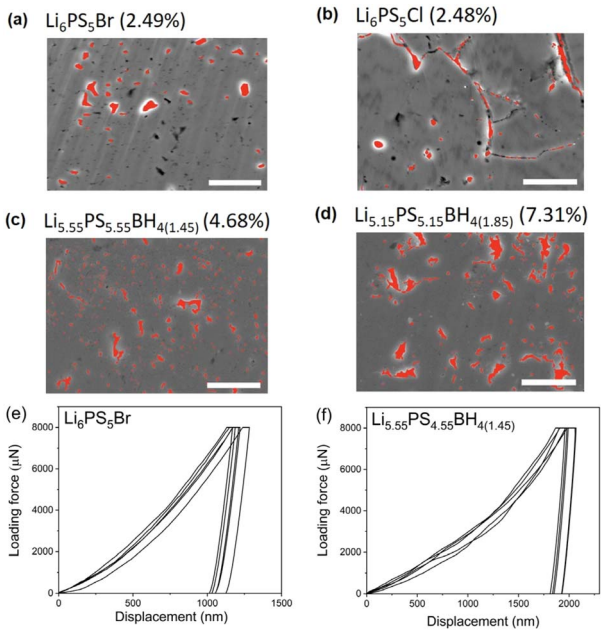

Fig. 3 (a–d) Porosity of cross-sections of different types of solid electrolyte pellets measured by SEM. The scale bar is 3 μm. The black spot, which resembles a pore-like feature, is an artifact caused by the 'edge effect,' as explained in detail in Fig. S3.† (e and f) Indentation curve of a synthesized sample. Measurements were taken at least five times at different locations for each sample.

indicates that the BH_4^- substituted SE powders proceed with easier plastic deformation due to lower hardness and yield stress compared to Li_6PS_5Cl and Li_6PS_5Br. As a result, a lower stress is required to fill up the voids, leading to the transition to stage III at relatively lower compressive stress for BH_4-substituted SE powders compared to Li_6PS_5Cl and Li_6PS_5Br.

The H/E ratio (plasticity index) can be derived from the hardness and elastic modulus obtained *via* nanoindentation.[38–40,42–44] A higher value of H/E means that the material is more capable of absorbing greater energy in the elastic region, resulting in reduced plastic deformation. Li_6PS_5Cl typically exhibits a value of approximately 5.0×10^{-2}, which aligns well with our result of 5.1×10^{-2}.[38–40,42–44] As shown in Table 2, a comparison of the H/E values of various electrolytes reveals that Li_6PS_5Br has the highest value of 5.5×10^{-2}, whereas $Li_{5.55}PS_{4.55}(BH_4)_{1.45}$ displays the lowest value of 3.5×10^{-2}. It is clear that the H/E is proportional to the inverse of the slope K from the Heckel plot. The H/E ratio, which reflects the balance between elasticity and plasticity, highlights that BH_4^--substituted SEs have a higher tendency for plastic deformation, making them mechanically softer and more adaptable for densification during pellet formation. Therefore, it is concluded that the powder compression test is an effective method to evaluate the relative plasticity of solid electrolyte powders for all-solid-state batteries.

Conclusions

In this study, the mechanical behavior of argyrodite-type solid electrolyte powders with different chemical compositions was investigated and compared using both the powder compression and nano-indentation tests. These findings highlight the necessity of considering the mechanical properties, such as the elastic modulus and hardness, when selecting SEs. While lower values may facilitate manufacturability by reducing the required compression stress, it is nevertheless crucial to ensure that the material exhibits adequate stiffness and hardness in order to maintain structural integrity and prevent mechanical failures during battery operation. The presence of voids within solid electrolyte membrane layers during the manufacturing process, as well as under in-service conditions, is a critical issue which may significantly affect the performance and reliability of the cell. Therefore, in the manufacturing process of ASSBs, it is crucial to densify the electrolyte membrane close to the theoretical density. It would be advantageous to select powders with uniform and finer sizes, a higher elastic modulus, and a lower yield stress. On the other hand, the yield stress and the elastic modulus should be high enough to prevent short circuits induced by mechanical damage throughout the entire life in service. A simple powder compression test described in the present study is a quite useful method to compare basic mechanical properties of different solid electrolyte powders and is believed to be helpful in selecting appropriate conditions in the manufacturing process of solid electrolyte membranes for ASSBs.

Data availability

The data supporting this article have been included as part of the ESI.†

Author contributions

Seung-Yong Lee and Ji-Hoon Han contributed equally to the preparation of this manuscript. Seung-Yong Lee contributed to the data curation, conceptualisation, formal analysis, investigation, validation, visualisation, and writing of the original draft. Ji-Hoon Han contributed to the data curation, conceptualisation, formal analysis, investigation, validation, visualisation, and writing the original draft. Hyun-Woo Gong contributed to the data curation. Jae-Pyung Ahn contributed to the data curation. Kyung-Woo Yi contributed to the supervision. Young Whan Cho contributed to the data curation, conceptualisation, formal analysis, investigation, validation, and writing of the original draft.

Conflicts of interest

There are no conflicts to declare.

Notes and references

1 N. Kamaya, K. Homma, Y. Yamakawa, M. Hirayama, R. Kanno, M. Yonemura, T. Kamiyama, Y. Kato, S. Hama, K. Kawamoto and A. Mitsui, *Nat. Mater.*, 2011, **10**, 682–686.
2 J. M. Tarascon and M. Armand, *Nature*, 2001, **414**, 359–367.

3 C. W. Sun, J. Liu, Y. D. Gong, D. P. Wilkinson and J. J. Zhang, *Nano Energy*, 2017, **33**, 363–386.
4 S. Chen, D. Xie, G. Liu, J. P. Mwizerwa, Q. Zhang, Y. Zhao, X. Xu and X. Yao, *Energy Storage Mater.*, 2018, **14**, 58–74.
5 Y. Kato, S. Hori, T. Saito, K. Suzuki, M. Hirayama, A. Mitsui, M. Yonemura, H. Iba and R. Kanno, *Nat. Energy*, 2016, **1**, 16030.
6 A. Sakuda, A. Hayashi and M. Tatsumisago, *Sci. Rep.*, 2013, **3**, 2261.
7 J.-M. Doux, Y. Yang, D. H. S. Tan, H. Nguyen, E. A. Wu, X. Wang, A. Banerjee and Y. S. Meng, *J. Mater. Chem. A*, 2020, **8**, 5049–5055.
8 W. D. Jung, J. S. Kim, Y. J. Kim, H. Jeong, D. Han, K. W. Nam, D. Ahn, D. H. Kwon, H. G. Jung, J. H. Lee and H. Kim, *Adv. Funct. Mater.*, 2023, **33**, 2211185.
9 L. L. Baranowski, C. M. Heveran, V. L. Ferguson and C. R. Stoldt, *ACS Appl. Mater. Interfaces*, 2016, **8**, 29573–29579.
10 Z. Fu and E. Wachsman, *J. Am. Ceram. Soc.*, 2023, **107**, 1481–1489.
11 G. Liu, W. Weng, Z. Zhang, L. Wu, J. Yang and X. Yao, *Nano Lett.*, 2020, **20**, 6660–6665.
12 D. K. Singh, A. Henss, B. Mogwitz, A. Gautam, J. Horn, T. Krauskopf, S. Burkhardt, J. Sann, F. H. Richter and J. Janek, *Cell Rep. Phys. Sci.*, 2022, **3**, 101043.
13 W. Zhang, D. A. Weber, H. Weigand, T. Arlt, I. Manke, D. Schroder, R. Koerver, T. Leichtweiss, P. Hartmann, W. G. Zeier and J. Janek, *ACS Appl. Mater. Interfaces*, 2017, **9**, 17835–17845.
14 Y. Wang and W. H. Zhong, *ChemElectroChem*, 2014, **2**, 22–36.
15 Y. Huang, L. Zhao, L. Li, M. Xie, F. Wu and R. Chen, *Adv. Mater.*, 2019, **31**, e1808393.
16 M. Cronau, M. Szabo, C. König, T. B. Wassermann and B. Roling, *ACS Energy Lett.*, 2021, **6**, 3072–3077.
17 S. Kalnaus, N. J. Dudney, A. S. Westover, E. Herbert and S. Hackney, *Science*, 2023, 381.
18 Y. Liu, H. Su, Y. Zhong, M. Zheng, Y. Hu, F. Zhao, J. T. Kim, Y. Gao, J. Luo, X. Lin, J. Tu and X. Sun, *Adv. Energy Mater.*, 2024, **14**, 2400783.
19 X. Feng, P.-H. Chien, Y. Wang, S. Patel, P. Wang, H. Liu, M. Immediato-Scuotto and Y.-Y. Hu, *Energy Storage Mater.*, 2020, **30**, 67–73.
20 L. Zhou, A. Assoud, Q. Zhang, X. Wu and L. F. Nazar, *J. Am. Chem. Soc.*, 2019, **141**, 19002–19013.
21 W. D. Jung, J. S. Kim, S. Choi, S. Kim, M. Jeon, H. G. Jung, K. Y. Chung, J. H. Lee, B. K. Kim, J. H. Lee and H. Kim, *Nano Lett.*, 2020, **20**, 2303–2309.
22 K.-H. Ni, Z.-L. Chen and C.-C. Li, *Acta Mater.*, 2024, **275**, 120057.
23 J. Wu, W. Chen, B. Hao, Z. J. Jiang, G. Jin and Z. Jiang, *Small*, 2024, e2407983.
24 M. D'Amore, L. E. Daga, R. Rocca, M. F. Sgroi, N. L. Marana, S. M. Casassa, L. Maschio and A. M. Ferrari, *Phys. Chem. Chem. Phys.*, 2022, **24**, 22978–22986.
25 Z. Deng, Z. Wang, I.-H. Chu, J. Luo and S. P. Ong, *J. Electrochem. Soc.*, 2015, **163**, A67–A74.
26 Z. Q. Wang, M. S. Wu, G. Liu, X. L. Lei, B. Xu and C. Y. Ouyang, *Int. J. Electrochem. Sci.*, 2014, **9**, 562–568.
27 I. M. B. Donald Peckner, *Handbook of Stainless Steels*, McGraw-Hill Book Company, New York, 1977.
28 T. L. G. H. E. Boyer, *Metals Handbook*, American Society for Metals, Metals Park, Ohio, 1985.
29 A. I. H. C. J. R. Davis, *Metals Handbook. Volume 1, Properties and Selection : Irons, Steels, and High-Performance Alloys*, ASM International, Materials Park, OH, 10 edn, 1990.
30 P. D. Harvey, *Engineering Properties of Steel*, American Society for Metals, Metals Park, Ohio, 1982.
31 C. Schneider, C. P. Schmidt, A. Neumann, M. Clausnitzer, M. Sadowski, S. Harm, C. Meier, T. Danner, K. Albe, A. Latz, W. A. Wall and B. V. Lotsch, *Adv. Energy Mater.*, 2023, **13**.
32 A. Hassanpour and M. Ghadiri, *Powder Technol.*, 2004, **141**, 251–261.
33 C. Sun and D. J. Grant, *Pharm. Dev. Technol.*, 2001, **6**, 193–200.
34 M. U. Ghori and B. R. Conway, *Br. J. Pharm.*, 2016, **1**, 19–29.
35 R. W. Heckel, *Trans. Metall. Soc. AIME*, 1961, **221**, 1001–1008.
36 P. Paronen, *Drug Dev. Ind. Pharm.*, 1986, **12**, 1903–1912.
37 J. M. Sonnergaard, *Int. J. Pharm.*, 1999, **193**, 63–71.
38 Y. T. Cheng and C. M. Cheng, *Appl. Phys. Lett.*, 1998, **73**, 614–616.
39 R. Yang, T. H. Zhang and Y. H. Feng, *J. Mater. Res.*, 2010, **25**, 2072–2077.
40 R. Yang, T. H. Zhang, P. Jiang and Y. L. Bai, *Appl. Phys. Lett.*, 2008, **92**.
41 J. Musil, F. Kunc, H. Zeman and H. Poláková, *Surf. Coat. Technol.*, 2002, **154**, 304–313.
42 O. Tutusaus, J. Hempel, S. Thapa, K. Kim, K. E. Kweon, B. C. Wood, L. Hentz, R. C. Hill, R. Mohtadi and Y.-T. Cheng, *PRiME*, 2024.
43 B. D. Beake, *Surf. Coat. Technol.*, 2022, **442**, 128272.
44 F. M. El-Hossary, A. M. Abd El-Rahman, M. Raaif and D. A. Ghareeb, *Appl. Phys. A:Mater. Sci. Process.*, 2016, **122**, 242.

